JACS
JOURNAL OF THE AMERICAN CHEMICAL SOCIETY

Article

Cite This: J. Am. Chem. Soc. 2019, 141, 19879−19887

pubs.acs.org/JACS

Operando Insight into the Correlation between the Structure and Composition of CuZn Nanoparticles and Their Selectivity for the Electrochemical CO_2 Reduction

Hyo Sang Jeon,[†] Janis Timoshenko,[†] Fabian Scholten,[†] Ilya Sinev,[‡] Antonia Herzog,[†] Felix T. Haase,[†] and Beatriz Roldan Cuenya*[,†]

[†]Department of Interface Science, Fritz-Haber Institute of the Max-Planck Society, 14195 Berlin, Germany

[‡]Department of Physics, Ruhr-University Bochum, 44780 Bochum, Germany

Supporting Information

ABSTRACT: Bimetallic CuZn catalysts have been recently proposed as alternatives in order to achieve selectivity control during the electrochemical reduction of CO_2 (CO_2RR). However, fundamental understanding of the underlying reaction mechanism and parameters determining the CO_2RR performance is still missing. In this study, we have employed size-controlled (∼5 nm) $Cu_{100-x}Zn_x$ nanoparticles (NPs) supported on carbon to investigate the correlation between their structure and composition and catalytic performance. By tuning the concentration of Zn, a drastic increase in CH_4 selectivity [∼70% Faradaic efficiency (F.E.)] could be achieved for Zn contents from 10 to 50, which was accompanied by a suppression of the H_2 production. Samples containing a higher Zn concentration displayed significantly lower CH_4 production and an abrupt switch in the selectivity to CO. Lack of metal leaching was observed based on quasi in situ X-ray photoelectron spectroscopy (XPS). *Operando* X-ray absorption fine structure (XAFS) spectroscopy measurements revealed that the alloying of Cu atoms with Zn atoms takes place under reaction conditions and plays a determining role in the product selectivity. Time-dependent XAFS analysis showed that the local structure and chemical environment around the Cu atoms continuously evolve during CO_2RR for several hours. In particular, cationic Zn species initially present were found to get reduced as the reaction proceeded, leading to the formation of a CuZn alloy (brass). The evolution of the Cu−Zn interaction with time during CO_2RR was found to be responsible for the change in the selectivity from CH_4 over Cu-ZnO NPs to CO over CuZn alloy NPs. This study highlights the importance of having access to in depth information on the interplay between the different atomic species in bimetallic NP electrocatalysts under *operando* reaction conditions in order to understand and ultimately tune their reactivity.

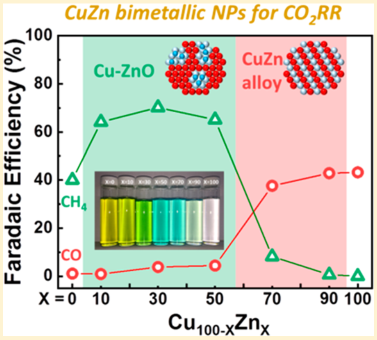

1. INTRODUCTION

The electrochemical reduction of CO_2 (CO_2RR) into useful chemicals and fuels has received much attention as a means to build carbon recycling systems.[1,2] However, efficient and inexpensive electrocatalysts are still required to reduce the thermodynamically stable CO_2 molecule while suppressing the H_2 evolution reaction (HER). While various metal surfaces (bulk foils) have been identified to efficiently reduce CO_2 into value-added carbon-based products such as CO (Au, Ag, and Zn), formic acid (Sn, In, and Bi), and hydrocarbons (Cu),[3] their catalytic activity, selectivity, and stability are still insufficient for industrial acceptance. In order to enhance the performance of metal catalysts, several strategies have been proposed, including nanostructuring the metals,[4−11] engineering the metal/electrolyte interface,[12−17] or introducing a secondary metal to create bimetallic structural motifs.[18−27]

The utilization of bimetallic catalysts has been considered a promising approach to obtain improved catalytic performance for CO_2RR.[28,29] CuZn is of particular interest due to its low cost and lack of toxicity. Recent studies have demonstrated enhanced reactivity of CuZn catalysts for CO_2RR.[30−36] For example, nanoporous CuZn catalysts prepared by annealing and subsequent reduction of commercial CuZn alloy foils showed four and six times higher Faradaic efficiency (F.E.) for CO and HCOOH than those of the untreated CuZn foils.[32] Zn-coated Cu electrodes exhibited higher selectivity for CH_4 (52% F.E.) than bare Cu (23% FE for CH_4).[33] Oxide-derived CuZn catalysts were favorable toward the formation of C_2 products (i.e., C_2H_4 and C_2H_5OH), and it was possible to tune the ratio of these products by varying the amount of Zn.[34] This trend in the C_2 selectivity was postulated to be due to the spillover of CO from Zn to Cu sites, which was thought to facilitate the production of C_2 products at the Cu site.[34] Such CO spillover effects were found to be facilitated when a homogeneous distribution of Cu and Zn atoms was formed in the CuZn catalysts.[35]

However, despite the former encouraging empirical results, significant discrepancies in the product selectivity of seemingly similar CuZn systems have been reported, and fundamental

Received: October 4, 2019
Published: November 24, 2019

DOI: 10.1021/jacs.9b10709
J. Am. Chem. Soc. 2019, 141, 19879−19887

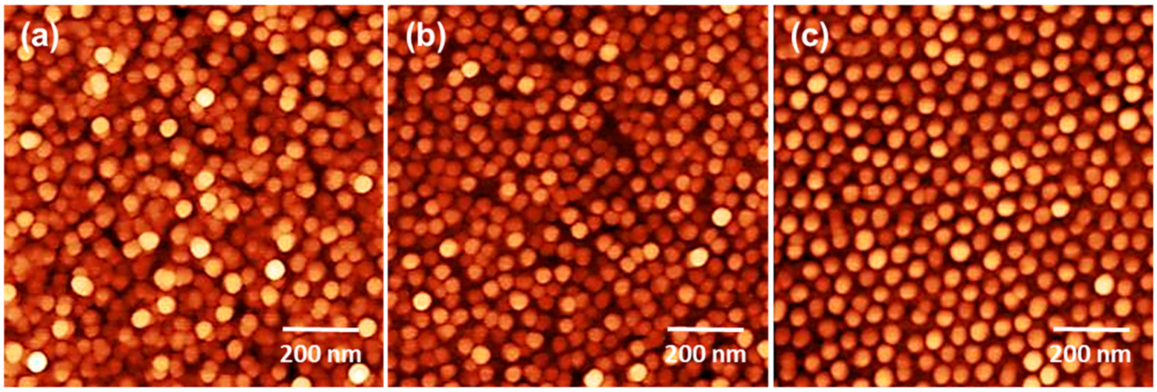

Figure 1. AFM images of $Cu_{100-x}Zn_x$ NPs supported on SiO_2/Si(111). (a) Cu_{100}, (b) $Cu_{50}Zn_{50}$, and (c) Zn_{100}.

understanding is still missing regarding the reaction pathways, catalyst structure, and composition leading to a given selectivity trend. Moreover, uncertainties remain concerning the relative importance of the different parameters that may be adjusted in order to tune the materials electrocatalytic performance. For the bulk CuZn catalysts previously investigated, grain boundaries,[37−39] local pH effects,[40−42] or the presence of cationic metal species[6,43−46] have been suggested to contribute to their altered product selectivity. However, the complexity of these material systems hinders our ability to disentangle the specific role of different parameters, which is required in order to understand the intrinsic reactivity of the CuZn system for CO_2RR.

In this work, morphologically and chemically well-defined ~5 nm CuZn nanoparticles (NPs) were synthesized via inverse micelle encapsulation and used to investigate the correlation between their structure, composition, and electrocatalytic activity and selectivity. By means of quasi in situ X-ray photoelectron spectroscopy (XPS) and *operando* X-ray absorption fine-structure spectroscopy (XAFS), the evolution of the structure, chemical state, and composition of the CuZn NPs was investigated under working CO_2RR conditions. The gradual formation of a Cu−Zn alloy could be observed in the course of the CO_2RR and correlated to the switch in selectivity from CH_4 to CO.

2. EXPERIMENTAL SECTION

2.1. Preparation of CuZn NPs. Bimetallic CuZn nanoparticles (NPs) with the same nominal NP size but variable composition were prepared by an inverse micelle encapsulation method.[47] The elemental composition was modified by controlling the molar ratio of the Cu and Zn precursor salts. $CuCl_2$ and $Zn(CH_3COO)_2$ were dissolved in a solution of toluene and tetrahydrofuran, followed by the addition of a second toluene solution with a poly(styrene)-*block*-poly(2-vinylpyridine) diblock copolymer (PS(48500)-P2VP(70000), Polymer Source, Inc.). The mixture was then stirred for 2 days. The encapsulated CuZn NPs were deposited on glassy carbon substrates. After deposition, an O_2-plasma etch treatment (20 W for 10 min, ~400 mTorr O_2) was used to remove the polymeric ligands. The specific synthesis parameters of the seven samples used in this study can be found in Table S1.

2.2. Morphological Characterization. Atomic force microscopy (AFM, Bruker, Multimode 8) was used to determine the NP height (h_p). The CuZn NPs were deposited on silicon wafers for more accurate measurement of h_p, since the glassy carbon electrode used for the electrochemical measurements has a rougher surface that makes difficult the background subtraction needed for the NP height determination. The average NP height was used to calculate the average CuZn geometric surface area of the NPs, $A_{CuZn} = 4\pi(h_p/2)^2$, assuming spherical micellar NPs. The metal NP surface area was then multiplied by the NP number density to estimate the total surface area of the CuZn NPs in each sample. This parameter was used for the normalization of the current data.

2.3. Electrochemical Characterization. Electrochemical CO_2 reduction experiments were conducted using an Autolab potentiostat (Multi Autolab M204) in an H-type two-compartment electrochemical cell made of polyether ether ketone (PEEK) separated by an anion-exchange membrane (Selemion AMV). A platinum mesh counter electrode and a leak-free Ag/AgCl reference electrode (Innovative Instruments) were used in a three electrode configuration. Purified 0.1 M $KHCO_3$ solutions were prepared by treating the electrolyte with Chelex 100 Resin (Bio-Rad). The electrolyte was saturated with CO_2 until a pH of 6.8 was achieved. Each data point presented corresponds to an identical freshly prepared sample measured with the chronoamperometric technique at −1.35 V versus RHE.

The gas products were quantified by gas chromatography (GC, Agilent 7890B) equipped with thermal conductivity (TCD) and flame ionization (FID) detectors. The GC was directly connected to the electrochemical cell for online gas analysis. CO_2 gas was bubbled through the electrolyte at an average rate of 20 mL min^{-1}. The formic acid concentration was analyzed by high-performance liquid chromatography (HPLC, Shimadzu Prominence) equipped with a NUCLEOGEL SUGAR 810 column and a refractive index detector (RID).

2.4. Structural and Chemical Characterization. Quasi in situ X-ray photoelectron spectroscopy (XPS) measurements were performed in an ultrahigh-vacuum setup equipped with a nonmonochromatic Al X-ray source ($h\nu$ = 1486.6 eV) and a hemispherical electron analyzer (Phoibos 100, SPECS GMbH). The XPS analysis chamber was connected to an electrochemical cell allowing sample transfer without exposure to air after electrochemistry. The measurements were conducted using an analyzer pass energy of E_{pass} = 13 eV and a source power of P = 300 W. All spectra were aligned to the carbon peak (E_{bin} = 284.8 eV) of the glassy carbon substrate. The composition ratio of Cu to Zn was calculated taking into account the relative sensitivity factors (RSF) of the metals (Cu $2p_{3/2}$: 20.28; Zn $2p_{3/2}$: 23.93) for an angle of 54° between the X-ray source and the analyzer and the transmission function of the analyzer.

Operando X-ray absorption fine-structure spectroscopy (XAFS) measurements were performed at the SAMBA beamline at SOLEIL synchrotron (France). A homemade electrochemical cell was used to acquire the XAFS spectra. All samples were measured in air and under *operando* conditions, while the potential was kept constant at −1.35 V versus RHE in a CO_2-saturated 0.1 M $KHCO_3$ electrolyte. XAFS spectra for the Cu *K*-edge (E_0 = 8979 eV) and Zn *K*-edge (E_0 = 9659 eV) were collected separately. Identically prepared (same NP solution) but different (fresh) samples were used for measurements at either the Cu or the Zn absorption edges. Further details of the XAFS measurements are given in the Supporting Information. Under CO_2RR conditions, multiple XAFS spectra were acquired, until there were no visible changes. This took several hours for these samples. Here we use time-dependent X-ray absorption near edge structure (XANES) data to follow the evolution of the sample structure and composition. We also analyzed extended X-ray absorption fine structure (EXAFS) data and compared the data obtained for samples in their as-prepared state in air and in their final state after several hours under applied potential. In addition to the evaluation of the XANES data, EXAFS spectra collected after 1 h CO_2RR under potential were also analyzed. Note, however, that the acquisition of a single EXAFS spectrum took ca. 12 min, which limits our time resolution. Moreover, due to the low signal-to-noise ratio, analysis of individual EXAFS spectra is problematic, and several spectra needed to be merged. Therefore, the representative EXAFS spectrum for a sample after 1 h of CO_2RR was obtained after merging 4 spectra collected during 40−80 min of CO_2RR.

Alignment, background subtraction, and normalization of the XAFS spectra were performed using the conventional approach as implemented in the Athena software.[48] Linear combination fitting was used to process the XANES data. To obtain quantitative information about the distributions of bond lengths, we performed Cu- and Zn *K*-edge EXAFS data fitting. Details of EXAFS data fitting are given in the Supporting Information.

3. RESULTS AND DISCUSSION

Figures 1 and S1 present AFM images of CuZn NPs with variable composition ratios. The AFM images show that all NPs exhibit spherical shape with uniform coverage across the substrate and narrow size distribution, with an average size of ca. 5 nm. Figure S2 displays the NP height histograms and the average values are included in Table S1. Following our previous work,[46] the metal NP coverage was chosen to be large enough (Table S1) so that the interparticle reactant diffusion and probability of readsorption of intermediates is not hindered.

In order to investigate the surface composition and chemical state of the CuZn NPs in their as-prepared state and after CO_2RR, quasi in situ XPS measurements were carried out. Figures 2 and S3 show the XPS spectra of the CuZn NPs in their as-prepared state and after CO_2RR. The surface composition ratio was obtained by integrating the areas of the Cu $2p_{3/2}$ and Zn $2p_{3/2}$ spectra. It was confirmed that the composition of the as-prepared samples was consistent with the starting molar ratio of the precursor salts, and that it did not change after the CO_2RR (Figure S4).

As shown in Figure 2a, Cu in the as-prepared samples after O_2-plasma treatment was found to be in Cu^{2+} state, as evidenced by the shakeup satellites.[47,49] After 1 h CO_2RR, the shakeup features vanished. Simultaneously, a shift of the Cu $2p_{3/2}$ main peak toward lower binding energies was observed (ΔE = 1.0 eV). Nevertheless, a ∼0.8 eV higher binding energy than that of bulk metallic Cu was observed after CO_2RR. This binding energy shift can be attributed to the initial and final state effects typically observed for small NPs.[49] We also attempted to detect the presence of Cu^+ species and distinguish them from Cu metal by using the Cu LMM Auger peak.[50] Unfortunately, the former signal for our low-metal coverage NP samples was beyond the detection limit. The Zn 2p region (Figures 2b and S3) shows that before CO_2RR the NPs are in the Zn^{2+} state (ZnO). The small change of 0.5 eV toward higher binding energies of the Zn $2p_{3/2}$ peak obtained after 1 h CO_2RR is attributed to the presence of $Zn(OH)_2$.[51]

Figure 3 shows the current density and F.E. for the CuZn NP samples as a function of their composition. As shown in Figure 3a, the Cu_{100} NPs exhibit the highest activity among all investigated samples, and the activity was found to monotonically decrease with increasing Zn content in the CuZn NPs. Interestingly, the F.E. of the CuZn NPs showed different selectivity during CO_2RR depending on the Cu to Zn ratio (Figure 3b). Cu_{100} and Zn_{100} NPs produced CH_4 and CO as the main products, respectively. The three $Cu_{100-x}Zn_x$ NPs (x = 10, 30, and 50) exhibited enhanced CH_4 F.E. compared to pure Cu NPs. Nonetheless, the increased CH_4 selectivity of these three samples was abruptly suppressed when the Zn content was higher than 70%, whereas CO selectivity was found to increase.

In order to further understand the reactivity of the CuZn NPs for CO_2RR, we also compared the partial current density of the major products as a function of the NP composition, as shown in Figure S5. Interestingly, we found that H_2 production showed a different trend depending on the CH_4 and CO production of the CuZn NPs. The H_2 production was significantly suppressed upon increasing the Zn concentration for the Cu-rich CH_4-producing CuZn NPs (i.e., $Cu_{90}Zn_{10}$, $Cu_{70}Zn_{30}$, and $Cu_{50}Zn_{50}$), while no changes in H_2 with Zn concentration were observed when the Zn-rich CO-producing CuZn NPs (i.e., $Cu_{30}Zn_{70}$ and $Cu_{10}Zn_{90}$) were considered. This result suggests that the protons that should be used to

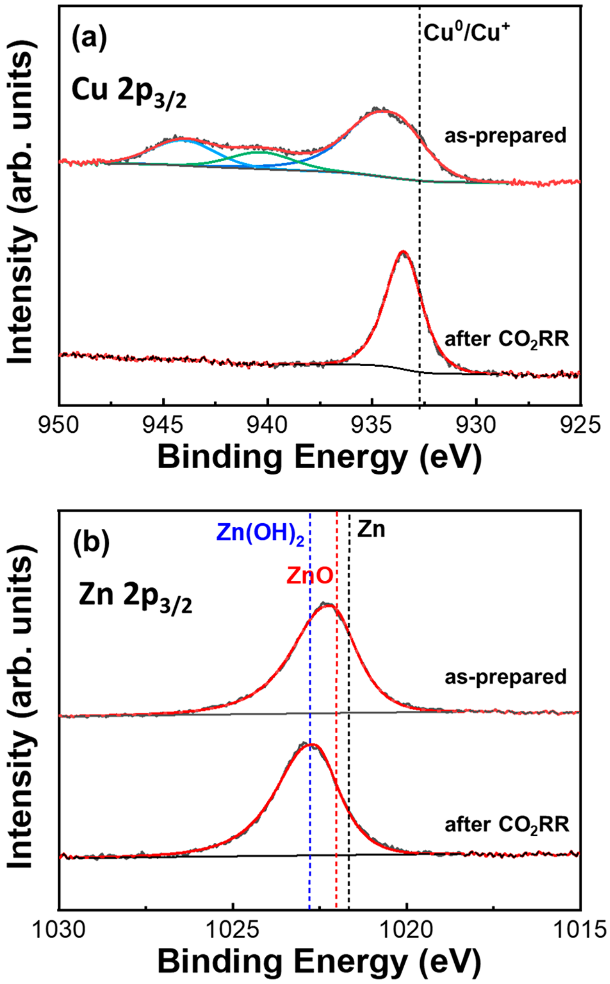

Figure 2. Quasi in situ XPS spectra of the (a) Cu $2p_{3/2}$ and (b) Zn $2p_{3/2}$ core level regions of $Cu_{50}Zn_{50}$ NPs deposited on glassy carbon acquired before and after (without air exposure) 1 h of CO_2RR at −1.35 V vs RHE.

DOI: 10.1021/jacs.9b10709
J. Am. Chem. Soc. 2019, 141, 19879−19887

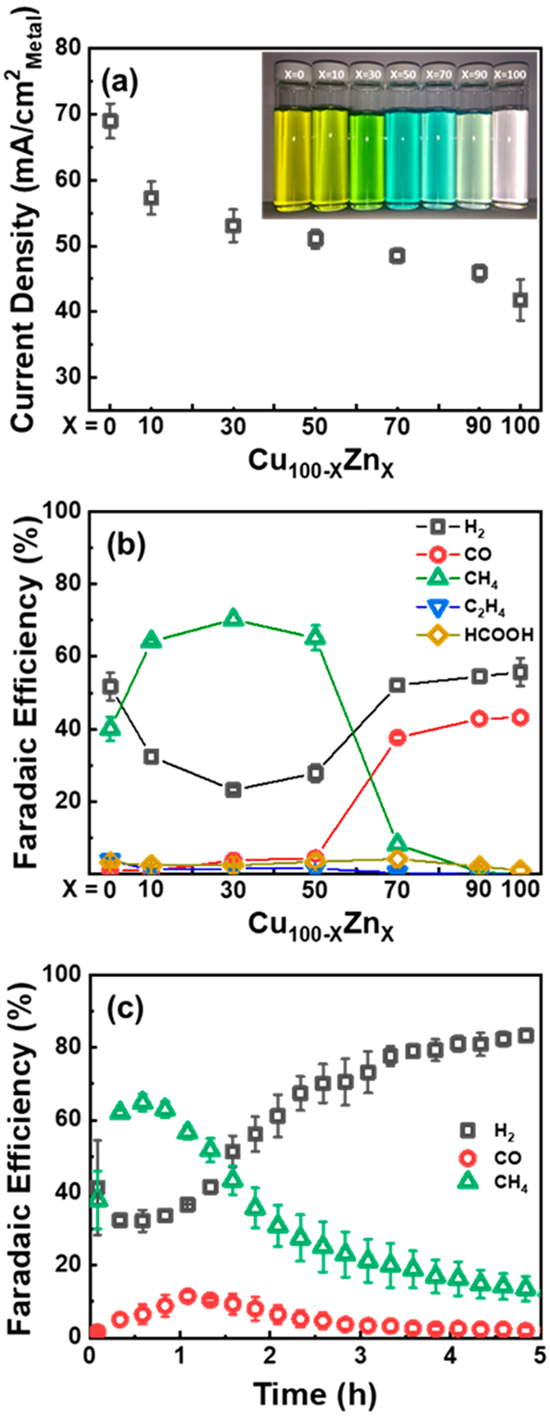

Figure 3. Activity and selectivity measurements of CO_2RR over $Cu_{100-x}Zn_x$ NPs. (a) Geometric current density and (b) Faradaic efficiency toward H_2, CO, CH_4, C_2H_4, and HCOOH measured during 1 h of electrolysis at −1.35 V vs RHE in 0.1 M $KHCO_3$ as a function of the NP composition. (c) Stability test of $Cu_{50}Zn_{50}$ NPs for the main products of CO_2RR at −1.35 V vs RHE as a function of time. The insert in (a) shows a photograph of the vials with the different CuZn NP solutions.

generate H_2 from water splitting have now a more favorable pathway toward CH_4 formation in the Cu-rich NPs.

In general, the product selectivity of CO_2 reduction is determined by the binding strength of adsorbed *CO and *H on the metal surface.[52,53] According to previous studies, since a bulk polycrystalline Cu electrode has a moderate binding energy for adsorbed *CO, such *CO species can be further hydrogenated to produce CH_4.[54−56] On the other hand, a relatively weak binding strength of adsorbed *CO is known for polycrystalline Zn electrodes, leading to CO production without further reaction.[34,35] These are also the main products detected for our monometallic Cu_{100} and Zn_{100} NP samples. However, it should be also considered that the enhanced fraction of low-coordinated atoms in NP samples such as those available here (5 nm) affect the relative binding of *H and *CO with respect to bulk systems of analogous composition, leading to distinct selectivity trends, in particular, enhanced H_2 production, as previously reported.[47,51] Interestingly, we found for our CuZn NPs increased CH_4 production as compared to Cu_{100} NPs. However, when the Zn content was higher than 70% in the bimetallic NPs, only CO and H_2 were produced. In the latter case, the proton and adsorbed *CO species that were not participating in the hydrogenation with adsorbed *CO on the Cu site may be released as H_2 and CO. Furthermore, the stability tests of the $Cu_{50}Zn_{50}$ sample showed that the enhanced CH_4 selectivity started to drop after 1 h, which is accompanied by a slight increase in CO selectivity (Figure 3c). This result indicates that the functionality of the Cu sites has changed over time.

To gain more detailed information about the chemical state and structure of the electrocatalysts during CO_2RR, XAFS measurements were conducted under *operando* conditions. Figure 4 shows selected Cu and Zn *K*-edge XANES spectra for $Cu_{50}Z_{50}$ NPs in their as-prepared state and under CO_2RR conditions. Similar plots for $Cu_{30}Zn_{70}$ and Zn_{100} samples are given in Figure S6. Complete sets of time-dependent XANES spectra for these samples are shown in Figure S7. The position of the absorption edge in the XANES spectra of the as-prepared samples and the direct comparison with the reference materials (Figure 4 and S8) indicate that the Cu and Zn components are initially completely oxidized and predominantly in the 2+ oxidation state. The local structure around the Cu atoms is similar to that in $Cu(OH)_2$, while from the Zn *K*-edge data we could not assign the observed XANES features to any particular reference material and can only conclude that some disordered oxide (or hydroxide) structure is formed.[51]

Under CO_2RR conditions, both Cu and Zn are reduced, as evidenced by the observed changes in the Cu and Zn *K*-edge XANES spectra, which become more similar to those of Cu and Zn foils (Figures 4 and S6−S7). Interestingly, the reduction rates appear to be very different for Cu and Zn. We observed that the Cu *K*-edge XANES spectra did not change much after the prompt initial reduction during the first scan under applied potential. However, at the Zn *K*-edge some variations in the XANES spectra for samples under potential were observed that had significantly longer characteristic times. To quantify these trends, we performed linear combination analysis using as reference the corresponding XANES spectra of the as-prepared sample (spectrum A in Figures 4a,b and S6), and the final spectrum (spectrum C in Figures 4a,b and S6) obtained after several hours under CO_2RR conditions. The results for different samples and absorption edges are compared in Figure 4c. It is evident that the reduction of ZnO species takes several hours, while that of the Cu oxide species is completed during the first XAFS scan within several minutes. In agreement with the quasi in situ XPS results, neither the Zn on the NP surface nor that inside the NP core is completely reduced after 1 h of CO_2RR. The reduction rate of Zn depends, however, on the $Cu_{100-x}Zn_x$ composition, with

DOI: 10.1021/jacs.9b10709
J. Am. Chem. Soc. 2019, 141, 19879−19887

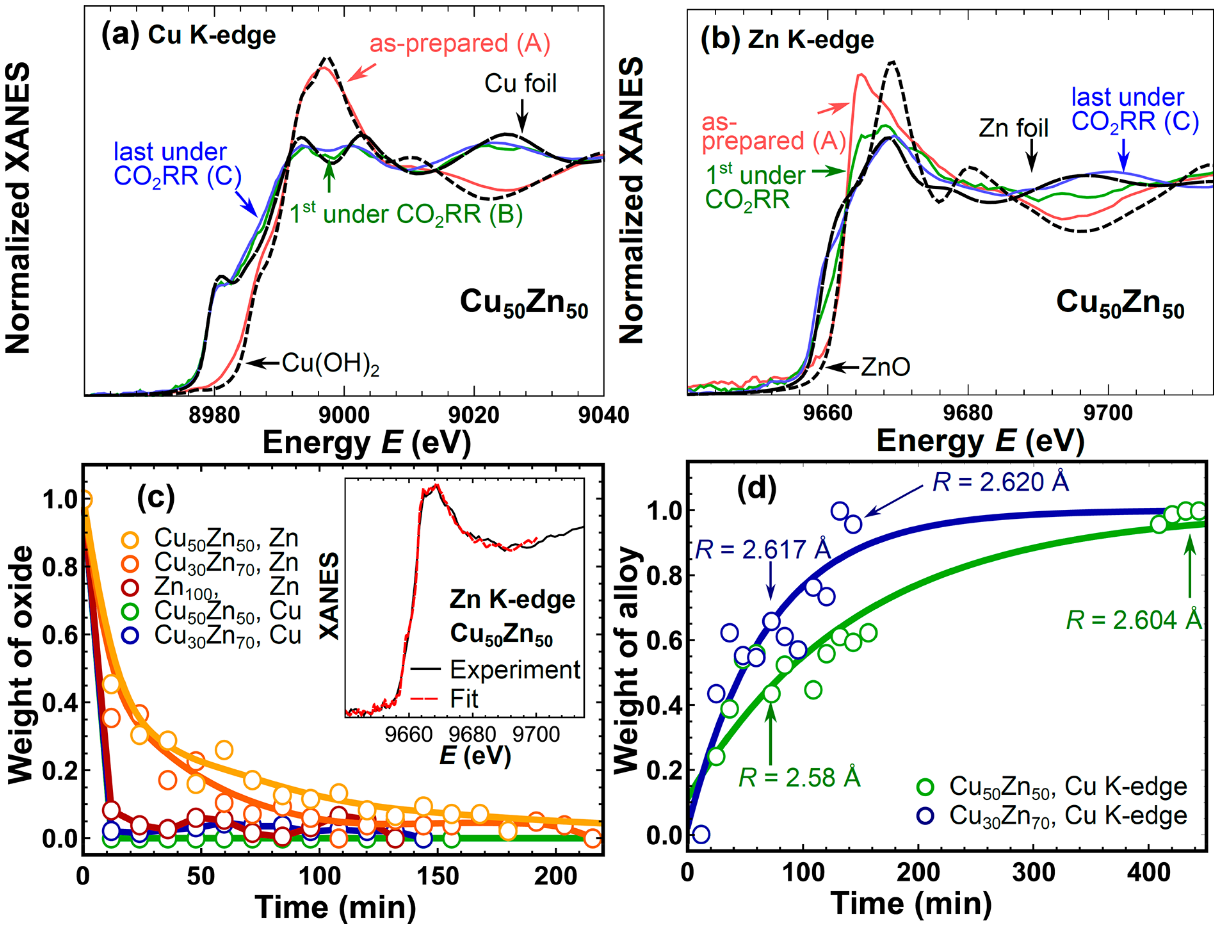

Figure 4. Selected (a) Cu *K*-edge and (b) Zn *K*-edge XANES spectra of $Cu_{50}Zn_{50}$ NPs corresponding to as-prepared oxidized samples (spectrum A), samples immediately after the onset of CO_2RR conditions (spectrum B) and the final spectrum collected after 7 h under CO_2RR conditions (spectrum C). (c) Linear combination analysis results for the Zn *K*-edge and Cu *K*-edge of XANES data of $Cu_{50}Zn_{50}$ and $Cu_{30}Zn_{70}$ NPs obtained using spectrum A (oxidized sample) and spectrum C (completely reduced sample) as reference. The inset shows a representative linear combination fit (result for Zn *K*-edge spectrum of $Cu_{50}Zn_{50}$ NPs immediately after the onset of CO_2RR conditions). (d) Linear combination analysis results of Cu *K*-edge XANES data using spectra B and C as reference, where the latter corresponds to the most alloyed state. Cu-M interatomic distances, as extracted from EXAFS data fitting, are also shown. Solid lines are guides for the eye.

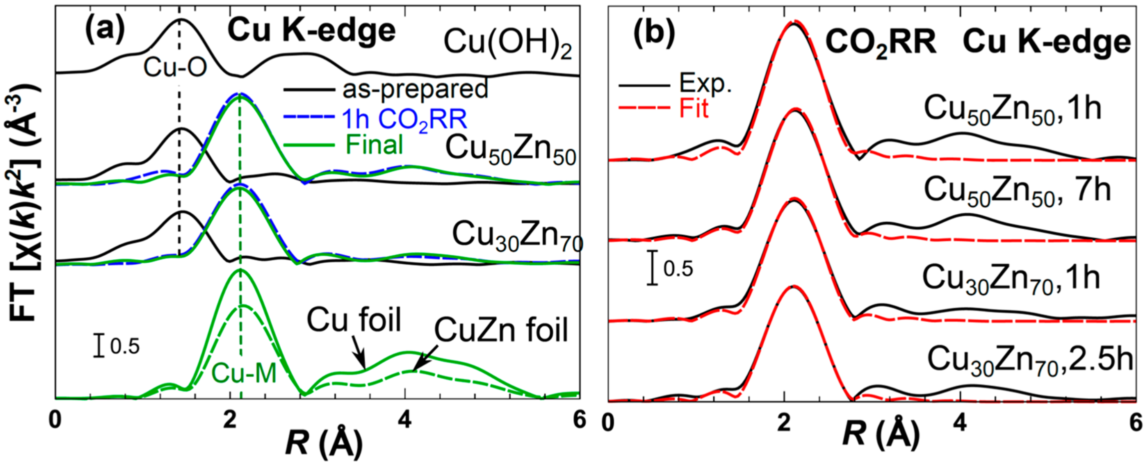

Figure 5. Fourier-transformed (FT) k^2-weighted Cu *K*-edge EXAFS data for $Cu_{50}Zn_{50}$ and $Cu_{30}Zn_{70}$ NPs measured (a) as-prepared in air, after 1 h of CO_2RR (dashed line) and in the final state (solid line). (b) EXAFS fitting results for $Cu_{50}Zn_{50}$ and $Cu_{30}Zn_{70}$ NPs under CO_2RR for the different times indicated. Reference spectra from a Cu foil, CuZn foil, and $Cu(OH)_2$ are also shown for comparison.

ZnO species in pure Zn NPs becoming reduced significantly faster than those in the bimetallic CuZn NPs. Since the Cu oxide species initially present in the small (~5 nm) NPs were found by XAFS to become reduced very promptly (within several minutes), they can be ruled out as responsible for the much slower change in the selectivity observed.

Even though the chemical state of the Cu species was stable (reduced) during the reaction, small variations in the Cu *K*-edge XANES spectra can still be observed, which can be linked to gradual changes in the local structure around Cu. To track these changes, linear combination analysis is employed, using in this case as references Cu *K*-edge XANES spectra corresponding to the final state (spectrum C in Figures 4a and S6b) and the first Cu *K*-edge XANES spectrum for a reduced sample (obtained after several minutes under CO_2RR conditions, spectrum B in Figures 4a and S6b). The obtained results, Figure 4d, demonstrate that the local structure around the Cu atoms continues evolving even after Cu is completely reduced. It should be noted that the characteristic times at which changes in the Cu *K*-edge XANES spectra are observed (Figure 4d) correlate well with the characteristic times of the reduction of the cationic Zn species (Figure 4c). Thus, from this observation, we can infer that the changes observed originate from the gradual enrichment of the samples with reduced Zn species and the interaction between the metallic Cu and metallic Zn species formed during CO_2RR.

To better understand the nature of the Cu−Zn interactions, EXAFS spectra, which are more sensitive to the geometry of the environment around the absorbing atoms, were analyzed. Fourier transformed (FT) Cu *K*-edge EXAFS spectra of $Cu_{50}Zn_{50}$, $Cu_{30}Zn_{70}$, and Zn_{100} NPs measured for the as-prepared samples, for samples after 1 h of CO_2RR and in the final state (after 7 h, 2.5 h, and 2 h of CO_2RR for $Cu_{50}Zn_{50}$, $Cu_{30}Zn_{70}$, and Zn_{100} NPs, correspondingly) are shown in Figure 5a (Cu-*K*-edge) and Figure S8a (Zn-*K*-edge). In agreement with the XANES data analysis, the FT-EXAFS spectra of the as-prepared samples reveal the presence of M−O (M = Cu and Zn) structural motifs, as evidenced by a strong peak at ca. 1.5 Å (phase uncorrected). Overall, the FT-EXAFS spectra for the Cu *K*-edge in the as-prepared samples are close to those of $Cu(OH)_2$.

Under CO_2RR conditions, the M−O peak disappears completely in the Cu *K*-edge data, while a strong peak at ca. 2.1−2.2 Å appears, which can be associated with the presence of M−M bonds. Thus, complete reduction of cationic Cu species in all CuZn samples is observed, in agreement with XANES data. Note here that since Cu and Zn are neighbors in the Periodic Table we cannot easily distinguish between Cu−Zn and Cu−Cu (or Zn−Zn and Zn−Cu) contributions. By comparing spectra obtained after 1 h of CO_2RR with the final spectra obtained after several hours of CO_2RR, small variations can be observed (more pronounced in the Zn *K*-edge data, Figure S9a), suggesting some gradual structural changes not only in the Zn but also in the Cu atomic environment.

For quantitative analysis, EXAFS data fitting was performed. For samples under CO_2RR conditions, Cu *K*-edge EXAFS fitting results are summarized in Figure 5b and in Table S2. The fitting results of the Cu and Zn *K*-edge EXAFS data of the as-prepared samples are presented in the Figure S9b−d and Tables S3 and S4. The main finding from the Cu *K*-edge EXAFS data analysis is that the Cu−M interatomic distance is different in $Cu_{50}Zn_{50}$ (2.58 ± 0.01 Å after 1 h under CO_2RR conditions) as compared to the $Cu_{30}Zn_{70}$ (2.617 ± 0.008 Å) NP sample (Table S2 and Figure 5b). Both distances are in between those of a Cu foil (2.56 Å) and a brass CuZn foil (2.62 Å), suggesting alloying of Cu with Zn. The increase of the interatomic distances in fcc-type Cu−Zn alloys with increasing Zn concentration is in agreement with X-ray diffraction data.[57] Moreover, the interatomic distances change with time. Table S2 provides the values of the fitting variables obtained for the $Cu_{30}Zn_{70}$ NPs after 2.5 h CO_2RR and for $Cu_{50}Zn_{50}$ NPS after 7 h. For both samples we observed an increase of the Cu−M distance with time, reaching 2.620 ± 0.008 Å for $Cu_{30}Zn_{70}$ NPs and 2.604 ± 0.008 Å for $Cu_{50}Zn_{50}$ NPs. In both cases the interatomic distances get closer to that in a CuZn brass foil. These time-dependent changes in interatomic distances can explain the observed time-dependent changes in the XANES spectra (Figure 4d) as well as the switch in the selectivity. Note that the sensitivity of the Cu *K*-edge XANES spectra to interatomic distance changes has been demonstrated in our recent work.[58] This allows us now to track the changes in the catalyst structure with better time-resolution than what was possible based on the EXAFS analysis. By combining insights from EXAFS and XANES data analyses, we conclude that the interaction (alloying) between the Cu and Zn atoms gradually takes place under CO_2RR conditions, and that it changes the local structure around the Cu atoms, making it more similar to that of bulk CuZn brass. Importantly, such changes took place in both samples ($Cu_{50}Zn_{50}$ and $Cu_{30}Zn_{70}$ NPs), but the local structure around Cu in the Zn-rich sample after 1 h of CO_2RR was already closer to that in the brass CuZn foil, as suggested by the larger Cu−M distance for this sample. Therefore, this result implies that the ratio of the Cu and Zn elements and their oxidation state is critical in determining both, the alloying degree immediately after the onset of the CO_2RR, as well as its evolution as a function of time.

Finally, based on the analysis of *operando* XAFS data we have observed a correlation between the product selectivity of the CuZn NPs and the reduction of the ZnO species and concomitant Cu−Zn alloy formation. It should be noted that there are a number of commonalities between the CO_2 electrochemical reduction and the CO_2 hydrogenation processes also taking place over Cu/ZnO catalysts, where the formation of brass might occur under certain reaction conditions and affect the catalytic selectivity. Since alloying in bimetallic systems induces the change of the geometric (or strain effect) structure, this transformation can lead to the tuning of the product selectivity in CuZn NPs. According to a recent experimental and theoretical study, an expansive strain in the Cu lattice should result in a more favorable stabilization of the reaction intermediates, leading to the formation of products beyond *CO.[49] This expansive Cu strain could explain the enhanced CH_4 selectivity in the Cu-rich CuZn NPs. Alloy formation, however, results also in a ligand effect and modification of the electronic structure, e.g., in a change of the *d*-band center of the metal atoms.[28,29] When upon reduction of the ZnO species a CuZn alloy is formed, the *d*-band center of Cu is shifted away from the Fermi level.[59] Such shift results in a weakening of the binding strength of *CO due to the occupancy of antibonding states.[18,60] Therefore, product selectivity in the Zn-rich CuZn NPs seems to be controlled by the ligand effect rather than strain effects, leading to the loss of the functionality of the Cu site for further reduction of CO intermediates.

Importantly, our time-dependent XAFS analysis revealed that alloying between Cu and Zn atoms gradually takes place upon reduction of the cationic Zn species. This fact explains why the selectivity of CO_2RR for CH_4 deteriorates over time. In fact, our durability data acquired for the $Cu_{50}Zn_{50}$ NPs showed that the concentration of the initially produced CH_4 gradually decreased after 1 h reaction (Figure 3c). In parallel, the concentration of CO slightly increased. This is assigned to the Cu−Zn alloy formation and the loss of the Cu site ability to hydrogenate adsorbed *CO. This result highlights the critical correlation of the structure and composition of the NP surface and the CO_2RR selectivity. Furthermore, it also implies that maintaining the metallic Cu-ZnO interface is vital for the stable production of CO_2 products, which can be affected by the reduction of the cationic Zn species in the CuZn alloyed catalysts. In conclusion, the product selectivity of CuZn NPs is determined by a combination of geometric and ligand effects, which become more or less prominent depending on the degree of alloying of the Cu−Zn species. In the first few hours, when the contribution of the Cu−Zn alloy is not significant, CH_4 formation over Cu-ZnO NPs is observed. Selectivity, however, switches to the formation of a CO+H_2 mix when brass is formed under CO_2RR conditions.[36]

Considering that our CuZn NP system was prepared as a model catalyst system, CH_4 and CO are the products to be expected when Cu is in contact with ZnO species within a nanoparticle. It is however known from previous studies that small Cu NPs favor CO production (and H_2) over hydrocarbons and alcohols.[61] Therefore, a comparison with other data in the literature on Cu−Zn systems must address two aspects: (i) whether a size effect should be considered and/or (ii) if the investigation has been conducted on a Cu-ZnO system or Cu−Zn alloy. Interestingly, several previous papers have reported the production of C_2 products such as ethylene and ethanol in CuZn catalysts containing Cu/ZnO or CuOx/ZnO species.[33,34] Others however reported only CO and H_2 production when the samples investigated consisted of Cu−Zn alloys already in the as-prepared state.[36] Our data serve to consolidate the different findings available in the Cu−Zn literature, in particular, to clarify that for bulk-like systems (films and large NPs), Cu−Zn alloys will lead to the exclusive production of CO and H_2, while dealloyed Cu/ZnO systems might also result in other products such as CH_4 for our NPs or even C_{2+} products for larger material systems.

4. CONCLUSION

In summary, we have demonstrated that the product selectivity of CuZn NPs can be correlated with the initial Cu/Zn ratio as well as with the degree of alloying between the Cu and Zn components, which was found to evolve under CO_2RR conditions. In particular, time-dependent XAFS data revealed that metallic Cu in close proximity to ZnO leads to the production of CH_4 at the initial stages of the reaction. The progressive reduction of the ZnO species taking place under CO_2RR conditions and the concomitant enhanced Cu−Zn interaction and brass alloy formation lead to the switch in the selectivity to the exclusive generation of CO and H_2. Our *operando* spectroscopy study provides crucial information on the nature of the active species and structure of CuZn NP catalysts. We believe that our findings can help to guide the rational design of bimetallic NP catalysts for CO_2RR.

■ ASSOCIATED CONTENT

Supporting Information

The Supporting Information is available free of charge at https://pubs.acs.org/doi/10.1021/jacs.9b10709.

XAS data and fitting results, AFM images, quasi *in situ* XPS spectra, and electrochemical data (PDF)

■ AUTHOR INFORMATION

Corresponding Author

*roldan@fhi-berlin.mpg.de

ORCID

Beatriz Roldan Cuenya: 0000-0002-8025-307X

Notes

The authors declare no competing financial interest.

■ ACKNOWLEDGMENTS

This work was funded by the German Federal Ministry of Education and Research (BMBF) under Grant 03SF0523C (CO2EKAT), the European Research Council under Grant ERC-OPERANDOCAT (ERC-725915), and the Deutsche Forschungsgemeinschaft (DFG, German Research Foundation) under Germany's Excellence Strategy, EXC 2008/1 (UniSysCat), 390540038.

■ REFERENCES

(1) Whipple, D. T.; Kenis, P. J. A. Prospects of CO_2 Utilization via Direct Heterogeneous Electrochemical Reduction. *J. Phys. Chem. Lett.* **2010**, *1*, 3451−3458.

(2) Kondratenko, E. V.; Mul, G.; Baltrusaitis, J.; Larrazabal, G. O.; Perez-Ramirez, J. Status and perspectives of CO_2 conversion into fuels and chemicals by catalytic, photocatalytic and electrocatalytic processes. *Energy Environ. Sci.* **2013**, *6*, 3112−3135.

(3) Hori, Y. Electrochemical CO_2 Reduction on Metal Electrodes. In *Modern Aspects of Electrochemistry*, Vayenas, C. G., White, R. E., Gamboa-Aldeco, M. E., Eds.; Springer: New York, NY, 2008; pp 89−189.

(4) Kim, C.; Jeon, H. S.; Eom, T.; Jee, M. S.; Kim, H.; Friend, C. M.; Min, B. K.; Hwang, Y. J. Achieving Selective and Efficient Electrocatalytic Activity for CO_2 Reduction Using Immobilized Silver Nanoparticles. *J. Am. Chem. Soc.* **2015**, *137*, 13844−13850.

(5) Mistry, H.; Choi, Y.-W.; Bagger, A.; Scholten, F.; Bonifacio, C. S.; Sinev, I.; Divins, N. J.; Zegkinoglou, I.; Jeon, H. S.; Kisslinger, K.; Stach, E. A.; Yang, J. C.; Rossmeisl, J.; Roldan Cuenya, B. Enhanced Carbon Dioxide Electroreduction to Carbon Monoxide over Defect-Rich Plasma-Activated Silver Catalysts. *Angew. Chem., Int. Ed.* **2017**, *56*, 11394−11398.

(6) Mistry, H.; Varela, A. S.; Bonifacio, C. S.; Zegkinoglou, I.; Sinev, I.; Choi, Y.-W.; Kisslinger, K.; Stach, E. A.; Yang, J. C.; Strasser, P.; Cuenya, B. R. Highly selective plasma-activated copper catalysts for carbon dioxide reduction to ethylene. *Nat. Commun.* **2016**, *7*, 12123.

(7) Loiudice, A.; Lobaccaro, P.; Kamali, E. A.; Thao, T.; Huang, B. H.; Ager, J. W.; Buonsanti, R. Tailoring Copper Nanocrystals towards C_2 Products in Electrochemical CO_2 Reduction. *Angew. Chem., Int. Ed.* **2016**, *55*, 5789−5792.

(8) Jeon, H. S.; Kunze, S.; Scholten, F.; Roldan Cuenya, B. Prism-Shaped Cu Nanocatalysts for Electrochemical CO_2 Reduction to Ethylene. *ACS Catal.* **2018**, *8* (1), 531−535.

(9) Li, Y.; Cui, F.; Ross, M. B.; Kim, D.; Sun, Y.; Yang, P. Structure-Sensitive CO_2 Electroreduction to Hydrocarbons on Ultrathin 5-fold Twinned Copper Nanowires. *Nano Lett.* **2017**, *17*, 1312−1317.

(10) Raciti, D.; Livi, K. J.; Wang, C. Highly Dense Cu Nanowires for Low-Overpotential CO_2 Reduction. *Nano Lett.* **2015**, *15*, 6829−6835.

(11) Saberi Safaei, T.; Mepham, A.; Zheng, X.; Pang, Y.; Dinh, C.-T.; Liu, M.; Sinton, D.; Kelley, S. O.; Sargent, E. H. High-Density Nanosharp Microstructures Enable Efficient CO_2 Electroreduction. *Nano Lett.* **2016**, *16*, 7224−7228.

(12) Lum, Y.; Yue, B.; Lobaccaro, P.; Bell, A. T.; Ager, J. W. Optimizing C−C Coupling on Oxide-Derived Copper Catalysts for Electrochemical CO_2 Reduction. *J. Phys. Chem. C* **2017**, *121*, 14191−14203.

(13) Singh, M. R.; Kwon, Y.; Lum, Y.; Ager, J. W.; Bell, A. T. Hydrolysis of Electrolyte Cations Enhances the Electrochemical

Reduction of CO_2 over Ag and Cu. *J. Am. Chem. Soc.* **2016**, *138*, 13006−13012.

(14) Gao, D.; Scholten, F.; Roldan Cuenya, B. Improved CO_2 Electroreduction Performance on Plasma-Activated Cu Catalysts via Electrolyte Design: Halide Effect. *ACS Catal.* **2017**, *7*, 5112−5120.

(15) Varela, A. S.; Ju, W.; Reier, T.; Strasser, P. Tuning the Catalytic Activity and Selectivity of Cu for CO_2 Electroreduction in the Presence of Halides. *ACS Catal.* **2016**, *6*, 2136−2144.

(16) Varela, A. S.; Kroschel, M.; Leonard, N. D.; Ju, W.; Steinberg, J.; Bagger, A.; Rossmeisl, J.; Strasser, P. pH Effects on the Selectivity of the Electrocatalytic CO_2 Reduction on Graphene-Embedded Fe−N−C Motifs: Bridging Concepts between Molecular Homogeneous and Solid-State Heterogeneous Catalysis. *ACS Energy Lett.* **2018**, *3*, 812−817.

(17) Resasco, J.; Chen, L. D.; Clark, E.; Tsai, C.; Hahn, C.; Jaramillo, T. F.; Chan, K.; Bell, A. T. Promoter Effects of Alkali Metal Cations on the Electrochemical Reduction of Carbon Dioxide. *J. Am. Chem. Soc.* **2017**, *139*, 11277−11287.

(18) Kim, D.; Resasco, J.; Yu, Y.; Asiri, A. M.; Yang, P. Synergistic geometric and electronic effects for electrochemical reduction of carbon dioxide using gold−copper bimetallic nanoparticles. *Nat. Commun.* **2014**, *5*, DOI: 10.1038/ncomms5948.

(19) Rasul, S.; Anjum, D. H.; Jedidi, A.; Minenkov, Y.; Cavallo, L.; Takanabe, K. A Highly Selective Copper−Indium Bimetallic Electrocatalyst for the Electrochemical Reduction of Aqueous CO_2 to CO. *Angew. Chem., Int. Ed.* **2015**, *54*, 2146−2150.

(20) Ma, M.; Hansen, H. A.; Valenti, M.; Wang, Z.; Cao, A.; Dong, M.; Smith, W. A. Electrochemical reduction of CO_2 on compositionally variant Au-Pt bimetallic thin films. *Nano Energy* **2017**, *42*, 51−57.

(21) Morales-Guio, C. G.; Cave, E. R.; Nitopi, S. A.; Feaster, J. T.; Wang, L.; Kuhl, K. P.; Jackson, A.; Johnson, N. C.; Abram, D. N.; Hatsukade, T.; Hahn, C.; Jaramillo, T. F. Improved CO_2 reduction activity towards C_{2+} alcohols on a tandem gold on copper electrocatalyst. *Nature Catal.* **2018**, *1*, 764−771.

(22) Luc, W.; Collins, C.; Wang, S.; Xin, H.; He, K.; Kang, Y.; Jiao, F. Ag−Sn Bimetallic Catalyst with a Core−Shell Structure for CO_2 Reduction. *J. Am. Chem. Soc.* **2017**, *139*, 1885−1893.

(23) Lu, L.; Sun, X.; Ma, J.; Yang, D.; Wu, H.; Zhang, B.; Zhang, J.; Han, B. Highly Efficient Electroreduction of CO_2 to Methanol on Palladium−Copper Bimetallic Aerogels. *Angew. Chem., Int. Ed.* **2018**, *57*, 14149−14153.

(24) Kortlever, R.; Peters, I.; Koper, S.; Koper, M. T. M. Electrochemical CO_2 Reduction to Formic Acid at Low Overpotential and with High Faradaic Efficiency on Carbon-Supported Bimetallic Pd−Pt Nanoparticles. *ACS Catal.* **2015**, *5*, 3916−3923.

(25) Cai, Z.; Wu, Y.; Wu, Z.; Yin, L.; Weng, Z.; Zhong, Y.; Xu, W.; Sun, X.; Wang, H. Unlocking Bifunctional Electrocatalytic Activity for CO_2 Reduction Reaction by Win-Win Metal−Oxide Cooperation. *ACS Energy Lett.* **2018**, *3*, 2816−2822.

(26) Clark, E. L.; Hahn, C.; Jaramillo, T. F.; Bell, A. T. Electrochemical CO_2 Reduction over Compressively Strained CuAg Surface Alloys with Enhanced Multi-Carbon Oxygenate Selectivity. *J. Am. Chem. Soc.* **2017**, *139*, 15848−15857.

(27) Sarfraz, S.; Garcia-Esparza, A. T.; Jedidi, A.; Cavallo, L.; Takanabe, K. Cu−Sn Bimetallic Catalyst for Selective Aqueous Electroreduction of CO_2 to CO. *ACS Catal.* **2016**, *6*, 2842−2851.

(28) Mistry, H.; Varela, A. S.; Kuhl, S.; Strasser, P.; Cuenya, B. R. Nanostructured electrocatalysts with tunable activity and selectivity. *Nat. Rev. Mater.* **2016**, *1*, 16009.

(29) Gao, D.; Arán-Ais, R. M.; Jeon, H. S.; Roldan Cuenya, B. Rational catalyst and electrolyte design for CO_2 electroreduction towards multicarbon products. *Nat. Catal.* **2019**, *2*, 198−210.

(30) Yin, G.; Abe, H.; Kodiyath, R.; Ueda, S.; Srinivasan, N.; Yamaguchi, A.; Miyauchi, M. Selective electro- or photo-reduction of carbon dioxide to formic acid using a Cu-Zn alloy catalyst. *J. Mater. Chem. A* **2017**, *5*, 12113−12119.

(31) Yin, G.; Sako, H.; Gubbala, R. V.; Ueda, S.; Yamaguchi, A.; Abe, H.; Miyauchi, M. A Cu-Zn nanoparticle promoter for selective carbon dioxide reduction and its application in visible-light-active Z-scheme systems using water as an electron donor. *Chem. Commun.* **2018**, *54*, 3947−3950.

(32) Hu, H.; Tang, Y.; Hu, Q.; Wan, P.; Dai, L.; Yang, X. J. In-situ grown nanoporous Zn-Cu catalysts on brass foils for enhanced electrochemical reduction of carbon dioxide. *Appl. Surf. Sci.* **2018**, *445*, 281−286.

(33) Keerthiga, G.; Chetty, R. Electrochemical Reduction of Carbon Dioxide on Zinc-Modified Copper Electrodes. *J. Electrochem. Soc.* **2017**, *164*, H164−H169.

(34) Ren, D.; Ang, B. S.-H.; Yeo, B. S. Tuning the Selectivity of Carbon Dioxide Electroreduction toward Ethanol on Oxide-Derived CuxZn Catalysts. *ACS Catal.* **2016**, *6*, 8239−8247.

(35) Feng, Y.; Li, Z.; Liu, H.; Dong, C.; Wang, J.; Kulinich, S. A.; Du, X. Laser-Prepared CuZn Alloy Catalyst for Selective Electrochemical Reduction of CO_2 to Ethylene. *Langmuir* **2018**, *34*, 13544−13549.

(36) Lamaison, S.; Wakerley, D.; Montero, D.; Rousse, G.; Taverna, D.; Giaume, D.; Mercier, D.; Blanchard, J.; Tran, H. N.; Fontecave, M.; Mougel, V. Zn-Cu Alloy Nanofoams as Efficient Catalysts for the Reduction of CO_2 to Syngas Mixtures with a Potential-Independent H_2/CO Ratio. *ChemSusChem* **2019**, *12*, 511−517.

(37) Li, C. W.; Kanan, M. W. CO_2 Reduction at Low Overpotential on Cu Electrodes Resulting from the Reduction of Thick Cu_2O Films. *J. Am. Chem. Soc.* **2012**, *134*, 7231−7234.

(38) Verdaguer-Casadevall, A.; Li, C. W.; Johansson, T. P.; Scott, S. B.; McKeown, J. T.; Kumar, M.; Stephens, I. E. L.; Kanan, M. W.; Chorkendorff, I. Probing the Active Surface Sites for CO Reduction on Oxide-Derived Copper Electrocatalysts. *J. Am. Chem. Soc.* **2015**, *137*, 9808−9811.

(39) Mariano, R. G.; McKelvey, K.; White, H. S.; Kanan, M. W. Selective increase in CO_2 electroreduction activity at grain-boundary surface terminations. *Science* **2017**, *358*, 1187−1192.

(40) Ma, M.; Djanashvili, K.; Smith, W. A. Controllable Hydrocarbon Formation from the Electrochemical Reduction of CO_2 over Cu Nanowire Arrays. *Angew. Chem.* **2016**, *128*, 6792−6796.

(41) Schouten, K. J. P.; Pérez Gallent, E.; Koper, M. T. M. The influence of pH on the reduction of CO and to hydrocarbons on copper electrodes. *J. Electroanal. Chem.* **2014**, *716*, 53−57.

(42) Kim, B.; Ma, S.; Molly Jhong, H.-R.; Kenis, P. J. A. Influence of dilute feed and pH on electrochemical reduction of CO_2 to CO on Ag in a continuous flow electrolyzer. *Electrochim. Acta* **2015**, *166*, 271−276.

(43) Favaro, M.; Xiao, H.; Cheng, T.; Goddard, W. A.; Yano, J.; Crumlin, E. J. Subsurface oxide plays a critical role in CO_2 activation by Cu(111) surfaces to form chemisorbed CO_2, the first step in reduction of CO_2. *Proc. Natl. Acad. Sci. U. S. A.* **2017**, *114*, 6706−6711.

(44) Choi, Y.-W.; Scholten, F.; Sinev, I.; Roldan Cuenya, B. Enhanced stability and CO/Formate selectivity of plasma-treated SnO_x/AgO_x catalysts during CO_2 electroreduction. *J. Am. Chem. Soc.* **2019**, *141*, 5261−5266.

(45) Lee, S. Y.; Jung, H.; Kim, N.-K.; Oh, H.-S.; Min, B. K.; Hwang, Y. J. Mixed Copper States in Anodized Cu Electrocatalyst for Stable and Selective Ethylene Production from CO_2 Reduction. *J. Am. Chem. Soc.* **2018**, *140*, 8681−8689.

(46) Mistry, H.; Behafarid, F.; Reske, R.; Varela, A. S.; Strasser, P.; Roldan Cuenya, B. Tuning catalytic selectivity at the mesoscale via interparticle interactions. *ACS Catal.* **2016**, *6*, 1075−1080.

(47) Mistry, H.; Reske, R.; Strasser, P.; Roldan Cuenya, B. Size-dependent reactivity of gold-copper bimetallic nanoparticles during CO_2 electroreduction. *Catal. Today* **2017**, *288*, 30−36.

(48) Ravel, B.; Newville, M. ATHENA, ARTEMIS, HEPHAESTUS: data analysis for X-ray absorption spectroscopy using IFEFFIT. *J. Synchrotron Radiat.* **2005**, *12*, 537−541.

(49) Bernal, M.; Bagger, A.; Scholten, F.; Sinev, I.; Bergmann, A.; Ahmadi, M.; Rossmeisl, J.; Cuenya, B. R. CO_2 electroreduction on copper-cobalt nanoparticles: Size and composition effect. *Nano Energy* **2018**, *53*, 27−36.

(50) Biesinger, M. C.; Payne, B. P.; Grosvenor, A. P.; Lau, L. W. M.; Gerson, A. R.; Smart, R. S. C. Resolving surface chemical states in XPS analysis of first row transition metals, oxides and hydroxides: Cr, Mn, Fe, Co and Ni. *Appl. Surf. Sci.* **2011**, *257*, 2717−2730.

(51) Jeon, H. S.; Sinev, I.; Scholten, F.; Divins, N. J.; Zegkinoglou, I.; Pielsticker, L.; Cuenya, B. R. Operando Evolution of the Structure and Oxidation State of Size-Controlled Zn Nanoparticles during CO_2 Electroreduction. *J. Am. Chem. Soc.* **2018**, *140*, 9383−9386.

(52) Kortlever, R.; Shen, J.; Schouten, K. J. P.; Calle-Vallejo, F.; Koper, M. T. M. Catalysts and Reaction Pathways for the Electrochemical Reduction of Carbon Dioxide. *J. Phys. Chem. Lett.* **2015**, *6*, 4073−4082.

(53) Zhang, Y.-J.; Sethuraman, V.; Michalsky, R.; Peterson, A. A. Competition between CO_2 Reduction and H_2 Evolution on Transition-Metal Electrocatalysts. *ACS Catal.* **2014**, *4*, 3742−3748.

(54) Peterson, A. A.; Abild-Pedersen, F.; Studt, F.; Rossmeisl, J.; Norskov, J. K. How copper catalyzes the electroreduction of carbon dioxide into hydrocarbon fuels. *Energy Environ. Sci.* **2010**, *3*, 1311−1315.

(55) Kuhl, K. P.; Cave, E. R.; Abram, D. N.; Jaramillo, T. F. New insights into the electrochemical reduction of carbon dioxide on metallic copper surfaces. *Energy Environ. Sci.* **2012**, *5*, 7050−7059.

(56) Manthiram, K.; Beberwyck, B. J.; Alivisatos, A. P. Enhanced Electrochemical Methanation of Carbon Dioxide with a Dispersible Nanoscale Copper Catalyst. *J. Am. Chem. Soc.* **2014**, *136*, 13319−13325.

(57) Owen, E. A.; Preston, G. D. X-ray analysis of zinc-copper alloys. *Proc. Phys. Soc.* **1923**, *36*, 49−66.

(58) Timoshenko, J.; Halder, A.; Yang, B.; Seifert, S.; Pellin, M. J.; Vajda, S.; Frenkel, A. I. Subnanometer Substructures in Nanoassemblies Formed from Clusters under a Reactive Atmosphere Revealed Using Machine Learning. *J. Phys. Chem. C* **2018**, *122*, 21686−21693.

(59) Andrews, P. T.; Hisscott, L. A. X-ray photoelectron spectroscopy of some Cu-Zn alloys. *J. Phys. F: Met. Phys.* **1975**, *5*, 1568−1572.

(60) Liu, K.; Ma, M.; Wu, L.; Valenti, M.; Cardenas-Morcoso, D.; Hofmann, J. P.; Bisquert, J.; Gimenez, S.; Smith, W. A. Electronic Effects Determine the Selectivity of Planar Au−Cu Bimetallic Thin Films for Electrochemical CO_2 Reduction. *ACS Appl. Mater. Interfaces* **2019**, *11*, 16546−16555.

(61) Reske, R.; Mistry, H.; Behafarid, F.; Roldan Cuenya, B.; Strasser, P. Particle Size Effects in the Catalytic Electroreduction of CO_2 on Cu Nanoparticles. *J. Am. Chem. Soc.* **2014**, *136*, 6978−6986.